Geophysical Journal International

3-D object-oriented image analysis of geophysical data

I. Fadel,[1,2] N. Kerle[1] and M. van der Meijde[1]

[1]*Faculty of Geo-Information Science and Earth Observation (ITC), University of Twente, P.O. Box* 217, *NL-7500 AE, Enschede, the Netherlands.*
E-mail: i.e.a.m.fadel@utwente.nl
[2]*Geology Department, Faculty of Science, Helwan University,* 11790 *Ain Helwan, Egypt*

SUMMARY

Geophysical data are the main source of information about the subsurface. Geophysical techniques are, however, highly non-unique in determining specific physical parameters and boundaries of subsurface objects. To obtain actual physical information, an inversion process is often applied, in which measurements at or above the Earth surface are inverted into a 2- or 3-D subsurface spatial distribution of the physical property. Interpreting these models into structural objects, related to physical processes, requires *a priori* knowledge and expert analysis which is susceptible to subjective choices and is therefore often non-repeatable. In this research, we implemented a recently introduced object-based approach to interpret the 3-D inversion results of a single geophysical technique using the available *a priori* information and the physical and geometrical characteristics of the interpreted objects. The introduced methodology is semi-automatic and repeatable, and allows the extraction of subsurface structures using 3-D object-oriented image analysis (3-D OOA) in an objective knowledge–based classification scheme. The approach allows for a semi-objective setting of thresholds that can be tested and, if necessary, changed in a very fast and efficient way. These changes require only changing the thresholds used in a so-called ruleset, which is composed of algorithms that extract objects from a 3-D data cube. The approach is tested on a synthetic model, which is based on *a priori* knowledge on objects present in the study area (Tanzania). Object characteristics and thresholds were well defined in a 3-D histogram of velocity versus depth, and objects were fully retrieved. The real model results showed how 3-D OOA can deal with realistic 3-D subsurface conditions in which the boundaries become fuzzy, the object extensions become unclear and the model characteristics vary with depth due to the different physical conditions. As expected, the 3-D histogram of the real data was substantially more complex. Still, the 3-D OOA-derived objects were extracted based on their velocity and their depth location. Spatially defined boundaries, based on physical variations, can improve the modelling with spatially dependent parameter information. With 3-D OOA, the non-uniqueness on the location of objects and their physical properties can be potentially significantly reduced.

Key words: Image processing; Seismic tomography; Cratons; Continental tectonics: extensional; Africa.

1 INTRODUCTION

Geophysical data are the main source of information about the subsurface. To obtain actual physical information an inversion process is applied, in which measurements at or above the Earth surface are inverted into a 2- or 3-D subsurface spatial distribution of the physical property related to these measurements (e.g. seismic wave subsurface distribution in case of seismic measurements). However, the resulting 3-D models need further interpretation to describe the subsurface lithological and structural components or to define the subsurface anomalous target, for example, mineral ore, fluid intrusion or specific target object.

It is well known that a single geophysical technique cannot determine the lithology, and that the usage of multiple geophysical techniques is more reliable due to the overlap between the different lithological units within the same range of values of the physical parameters, for example, limestone and granite have the same electrical conductivity values but differ in magnetic susceptibilities (Bedrosian 2007). A lot of work has been done on combining two or more geophysical techniques to define an explicit
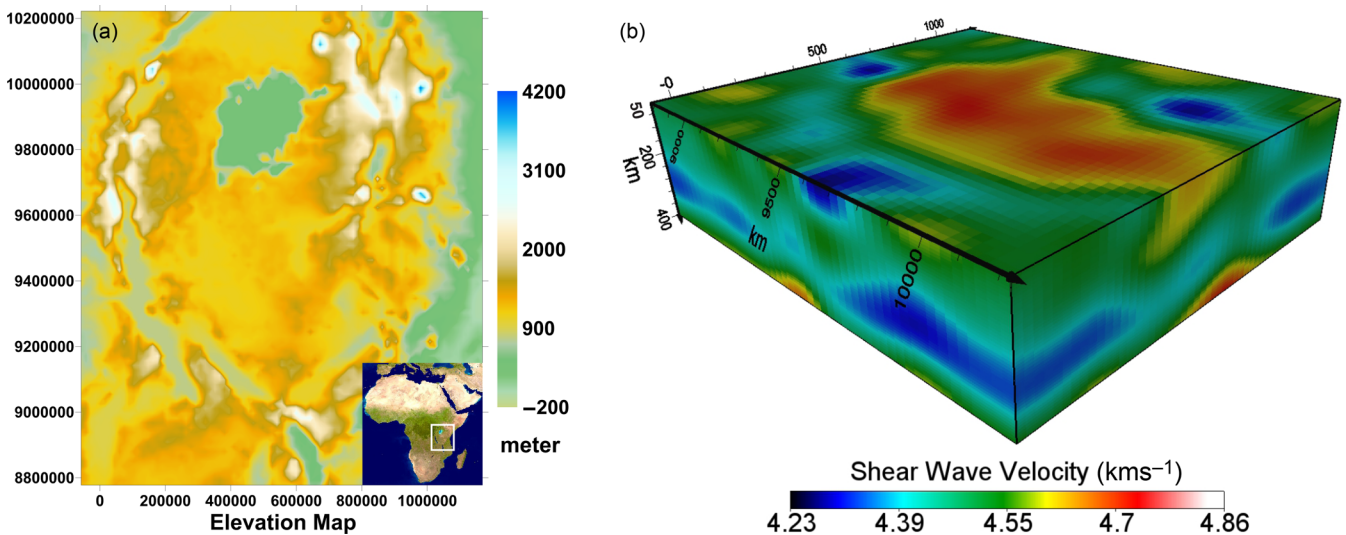
Figure 1. (a) Elevation map of the study area with inset map showing the location of the study area within Africa. (b) The shear wave tomography model of the study area. Adapted from Adams *et al.* (2012).

lithological interpretation of the studied areas, for example, Bosch (1999), Bedrosian *et al.* (2007), Guillen *et al.* (2008), Infante *et al.* (2010) and Bauer *et al.* (2012). The joint structural and lithological interpretation of different geophysical techniques was done based on pixel-by-pixel analysis for the correlated patterns in the resulting 3-D models, and assigning trends to distinct lithological units (Gallardo & Meju 2011). However, these approaches were focusing on defining specific ranges of physical parameters, for example, velocity and resistivity, for each classified subsurface object. They did not take in consideration other parameters such as depth or geometry, which can help in the classification process.

For a single geophysical technique, for example, seismic reflection/refraction or tomography, the interpretation and the classification have been done without a standardized methodology and were often done based on contouring or expert interpretation of the 3-D seismic velocity data cube and *a priori* information about the studied area (e.g. Ebbing *et al.* 2001; Li 2010; Sanchez *et al.* 2011). However, this can be sensitive to subjective choices that can often make the process unrepeatable. The mentioned approaches, either for single or joint interpretation techniques, were mainly voxel-based (the 3-D nomenclature of pixel). However, recent object-based analysis techniques have proven a superior performance over the pixel-based ones. However, to our knowledge, they were never applied in 3-D geophysical interpretation.

In this research, we implement a recently introduced object-based approach to interpret the 3-D inversion results of a single geophysical technique using the available *a priori* information and the physical and geometrical characteristics of the interpreted objects. The introduced methodology is semi-automatic and allows the extraction of subsurface structures using 3-D object-oriented image analysis (3-D OOA) in an objective knowledge–based classification scheme. 3-D OOA is an advanced image analysis technique that has originated in the biomedical field (Schönmeyer *et al.* 2006). To our knowledge, it is applied here for the first time to 3-D seismological data to identify 3-D objects. The study area in which we apply this methodology is the Tanzania Craton and surroundings. The method is first tested on a synthetic model that simulates the study area. Subsequently, it is used to extract 3-D subsurface objects from a real 3-D seismic tomographic model of the study area. However, it should be kept in mind that this work mainly targets the subsur-

face structures or objects which may not be the same as lithological classification, which needs more physical parameters to be done.

2 STUDY AREA

The study area is the central part of the East African Rift System (Fig. 1a) for which Adams *et al.* (2012) created a 3-D shear wave seismic tomography model. It is a voxel-based model that ranges from a depth of 50 km down to 400 km at 10-km increments. The subsurface model can be divided into two main parts (Adams *et al.* 2012). The upper part of the model (<∼200 km) is characterized by the high velocities of the Tanzanian Craton and the surroundings basement complex, and low velocities of the surrounding tectonic elements, such as rift branches, Proterozoic mobile belts and Cenozoic volcanism. The lower part is dominated by low velocities related to a plume head, or part of the deep mantle super plume in western Africa (see Adams *et al.* 2012, for more details about the 3-D shear wave tomography model).

3 METHODOLOGY

3.1 Synthetic model creation

The synthetic model is a 3-D voxel velocity model that was designed in IGMAS+ (3-D Interactive Gravity and Magnetic Application System, Götze & Lahmeyer 1988; Schmidt *et al.* 2010) based on the interpretation of the tomography model of the study area provided by Adams *et al.* (2012). The vertical and lateral dimensions are close to reality, and also the velocity variations of the different objects are physically realistic. It contains four main objects: craton (C), rift (R), plume (P) and three horizontal layers (L1, L2 and L3) (Fig. 2). The craton and rifts were equally divided into three zones (C1, C2 and C3, and R1, R2 and R3, respectively) to simulate increased velocity with depth (Fig. 2). Vertical gradual boundaries (RL and RC) were implemented to describe the transition from rifts to surroundings (either layers or craton, respectively), and a horizontal gradual diffuse boundary (PB) was defined between the plume and objects above. The model was gridded into depth slices using Ordinary Kriging, and subsequently converted into a 3-D
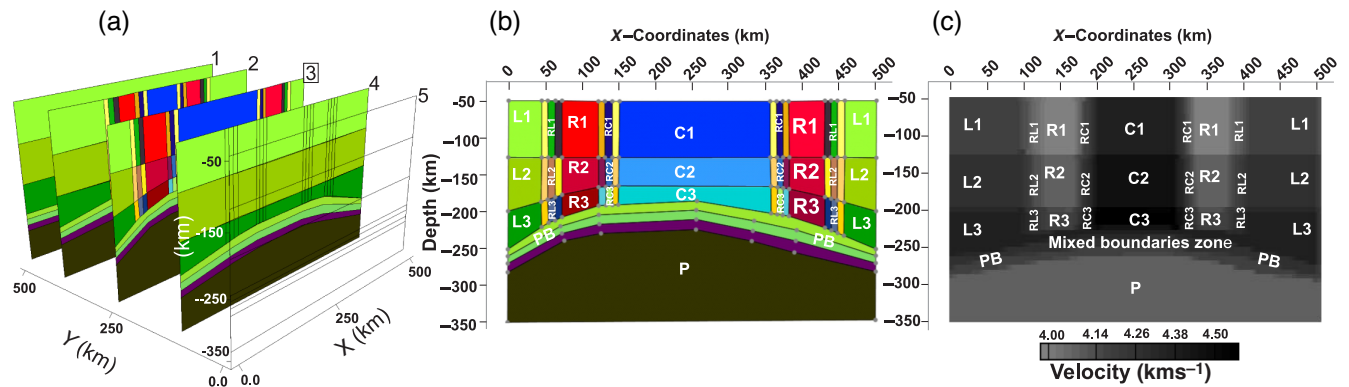
Figure 2. The composition of the synthetic model. (a) Five vertical sections that compose the synthetic models; (b) the detailed explanation of the objects vertical section number 3, the model elements are: rift (R), craton (C), layer (L), boundaries between rift and layers (RL), boundaries between rifts and craton (RC), boundaries between plume and upper objects (PB) and plume (P) (the colours of the section do not describe the velocity of the objects). (c) The detailed explanation of vertical section number 3 in the grey scale of the 3-D image stack.

image stack using XML code to be used for 3-D OOA in eCognition, the most widely used commercial OOA software package (Blaschke 2010, www.ecognition.com).

3.2 Real model preparation

The *S*-wave seismic tomography model (Fig. 1b) was converted into a 3-D image stack to be used in eCognition. It included 36 slices ranging from a depth of 50–400 km with a 10-km depth interval and 0.5° horizontal spacing in *X* and *Y*-directions. The slices were gridded using a grey scale colour scheme with a linear colour distribution, as commonly used in the biomedical field (e.g. Schönmeyer *et al.* 2006). Then they were converted into a 3-D image stack in the same way as the synthetic model.

3.3 3-D object-oriented analysis

In general terms, object-oriented analysis (OOA) is a two-step procedure, comprising image segmentation (creation of contiguous segments or objects that are relatively homogeneous in terms of adjacent pixel or point values), and their subsequent classification. The principal advantage over traditional pixel-based methods is that the generated segments are associated with attributes (e.g. spectral, textural, geometric, contextual or physical), which are employed in the object classification. OOA is thus a form of knowledge-driven analysis that mimics the approaches of cognitive visual image analysis (Kerle & de Leeuw 2009; Martha *et al.* 2011).

Released in 2000, eCognition was the first commercial OOA software, and has become the most frequently used tool, with some 50–55 per cent of all published scientific studies on OOA using it (Blaschke 2010). The segmentation/classification process in eCognition is implemented through rulesets. This allows complex processing schemes to be developed that can comprise a number of different segmentation and classification routines, supported by additional object refinement steps. The ruleset is semi-automatic since the used segmentation and classification algorithms are already developed and existing in eCognition package. The user needs only to define the optimum thresholds to define the target segmentation scheme or to extract the target object. 3-D OOA is a recent extension of these concepts, allowing the processing of data cubes such as created from laser scanning data (LiDAR) or tomographic analysis. The origins of this extension lie in the biomedical field, such as the processing of 3-D X-Ray computed tomography images (CT;

Schönmeyer *et al.* 2006). More recently, the technique has also been tested in the remote sensing community through an example of 3-D OOA processing of LiDAR point cloud data (Willhauck 2012).

Also in the 3-D domain, the process starts with the segmentation of an image stack into relatively homogenous segments that, together with their associated attributes, are used in the subsequent classification process. The main challenge facing OOA is the determination of the thresholds for both segmentation and classification steps, and the selection of suitable segment attributes. They usually are based on user interpretation (knowledge-driven), or on statistical data analysis techniques, such as Random Forests (Stumpf & Kerle 2011). In this work, the thresholds necessary for defining the 3-D objects are based on analysis of the 3-D histogram of velocity versus depth of the 3-D subsurface model, supported by *a priori* geological knowledge about the subsurface objects, available from previous studies. The inferred thresholds guided the segmentation and subsequent classification of the generated segments through different algorithms as summarized in Table 1.

4 RESULTS

4.1 3-D OOA of the synthetic model

The 3-D histogram of the synthetic model (Fig. 3) describes the distribution of velocity values with depth. The separability of different objects was used to define the main characteristics of the objects in the 3-D image stack (Fig. 2). The four main features of the synthetic model, the plume (P), craton (C), rift (R) and horizontal layering (L1, L2 and L3), can be identified in the 3-D histogram as distinct objects. The gradual boundaries between the main features (RL, RC and RB; Fig. 2) result in small features that are partly overlapping with the main features.

The cratonic parts (C1, C2 and C3) are distinguishable as three blocks with higher velocity values (4.575, 4.475 and 4.375 km s^{-1}, respectively) in the intermediate to shallow depth level. The plume (P) is visible on the opposite side of the histogram at the deep levels, but has a relatively low velocity. In between the rift (R1, R2 and R3) and the horizontal layers (L1, L2 and L3) are positioned. The rift, on average, has low-velocity values of 3.975, 4.075 and 4.175 km s^{-1} for the R1, R2 and R3 depth levels, respectively. The horizontal layers are located at the same depth intervals as the rifts, but have intermediate velocity values of 4.175, 4.275 and 4.375 km s^{-1} for layers 1, 2 and 3, respectively.

Table 1. An overview of applied segmentation and classification algorithms adapted from eCognition Developer (2011a,b).

Algorithm	Description
Multithreshold segmentation:	It splits the images into objects and classifies them based on pre-defined thresholds that can be user-defined or can be adapted with the combination of other automatic approaches.
Classification:	The classification algorithm evaluates the likelihood that an image object belongs to a specific class based on a class description that can be a threshold or membership function for one or a combination of the different object features. Those can be spectral, textural, geometrical or contextual features. The algorithm allows also the use of fuzzy logic conditions to describe such functions.
Assign Class:	The algorithm determines whether an object belongs to a class or not based on a single threshold condition.
Pixel-based object resizing:	It allows a user-defined object to grow, shrink or be coated in a user-defined direction (*x* and/or *y* and/or *z*), or a user-defined object class, or within specific pixel values. The coating option allows the coating pixels on objects to be classified into another class, which is different from the growing option that allows the object itself to grow in the surrounding pixels.
Merge region:	The algorithm merges adjacent segments belonging to the same class into one segment.
Convert image objects:	It connects the 2-D segments into 3-D segments.
Export view:	It exports the classification results with their georeference information into one of different raster formats, for example, jpeg or tif.
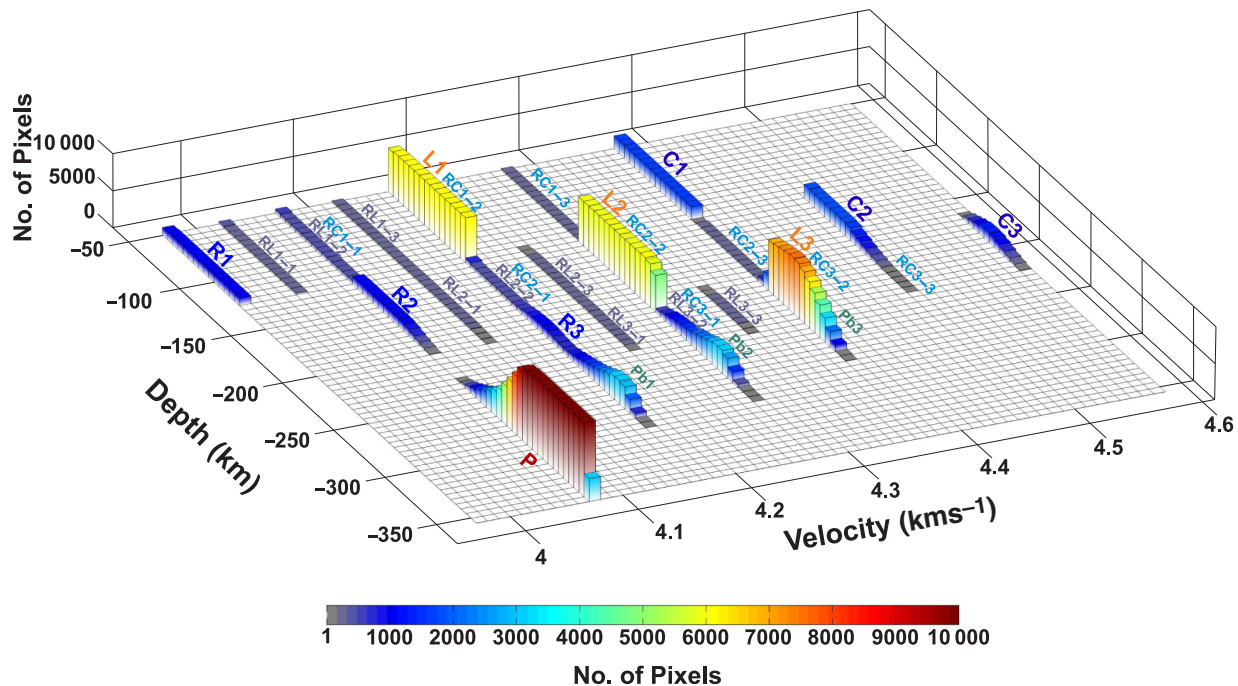
Figure 3. 3-D histogram of the synthetic model explaining the process of the object extraction based on the object velocity values and their depths. Rift (R), Craton (C), layer (L) boundaries between rift and layers (RL), boundaries between rift and craton (RC), boundaries between plume and upper objects (PB) and plume (P).

The complexity in the interpretation of the 3-D histogram comes from the gradual boundaries (RL, RC and PB) that have intermediate velocity values in between the four main features. The boundary between two objects was divided into three parts that have gradually changing velocity values. For example, RL1 (Fig. 2b) was divided into three parts RL1-1, RL1-2 and RL1-3 with velocity values of 4.025, 4.075 and 4.125 km s^{-1}, respectively. They describe the transition between the first level of the rift (R1: 3.975 km s^{-1}) and layer 1 (L1: 4.175 km s^{-1}) (see the 3-D histogram in Fig. 3). Some of these boundaries (Fig. 3) have a distinctly different velocity (e.g. RL1-1), some overlap with the velocity of other units and are only distinguishable in depth (e.g. C2 and RC3-3, and also RL1-2 and RC1-1), and some are overlapping in both velocity values and depth ranges (e.g. L1 and RC1-2, as well as L3, RC3-2 and PB3). Layers 1, 2 and 3 share the same velocity values and depth ranges with the boundaries between the craton and rift (RC1-2, RC2-2 and RC3-3, respectively). And although the rift boundaries at the different levels (RL1-1 to RL3-3 and RC1-1 to RC3-3) have a shallow depth (50–220 km), and the plume boundaries (PB1–PB3) have a deep location (190–295 km), there was a zone (190–220 km) in which both boundaries were mixed in depth but could be separated by velocity (Figs 2b and c).

The ruleset is based on these distinctions and often use a combination of velocity values and depth (Appendix S1, Supporting Information). The object extraction process was done in five steps.

In step 1, segments were created and classified based on velocity values through the *multithreshold segmentation* algorithm (Table 1). 11 thresholds were used to create the segments and classify them
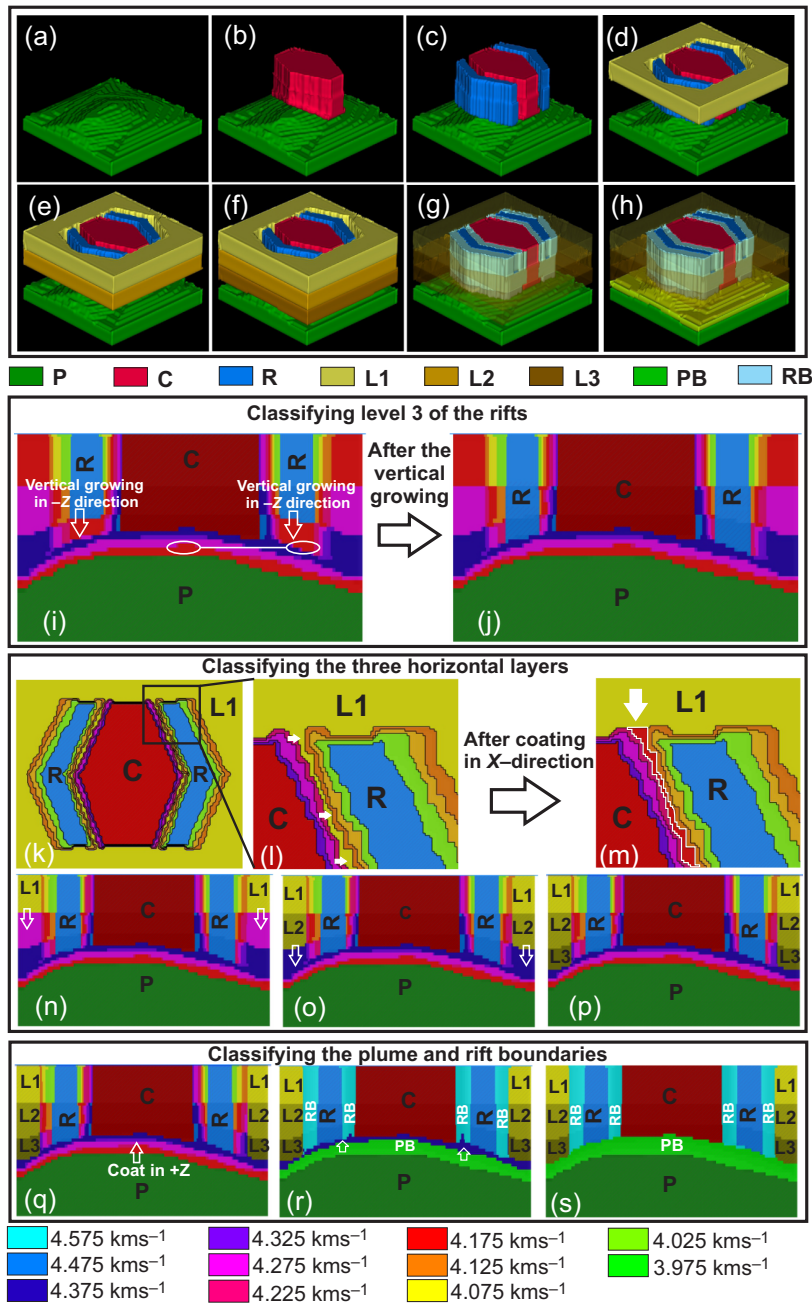
Figure 4. 3-D OOA of the synthetic model. Figs (a–h) show the 3-D OOA extraction process with the plume P (a), craton C (b), rifts R (c), layers L1, L2 and L3 (d, e and f, respectively, and displayed with 50 per cent transparency), the rift boundary RB (g) and the plume boundaries PB (h). Panels (i) and (j) (section 3 in Fig. 2) show the vertical growing process of the rift into the 4.175 km s^{-1} class. The white circles show the rift and plume boundaries that share the same velocity value and depth range. The white arrows indicate the growing process in $-Z$-direction. Panels (k), (l) and (m) (depth slice 60 km) show the process of correcting the misclassification in the rift boundaries during the classification of layer 1. (l) highlights the misclassified segment and the white arrows indicate the coating process in the X-direction. Panel (m) shows the corrected segment indicated by the white arrow and surrounded by white line. Panels (n), (o) and (p) (section 3) illustrate the classification of layers 2 and 3. Figure (n) shows layer 1 and the white arrow indicates the coating process in $-Z$-direction. The white arrows in (o) indicate the coating process of layer 2 in $-Z$-direction to define layer 3. (n) Layer 3 after the coating process. Figs (q), (r) and (s) (section 3) explain the process of classifying the rift and plume boundaries. Fig. (q) shows a white arrow that indicates the coating process of the plume in $+Z$-direction in order to define the plume boundaries. (r) plume and rift boundaries except 4.375 km s^{-1} class in blue colour, while the white arrow indicates the two-step growing process of the plume boundaries in order to define the plume boundaries in the 4.375 km s^{-1} class. (s) The final classification result.

into 12 velocity classes based on the histograms of the 3-D image stack (Fig. 3).

Step 2 classified the plume and the craton based on their velocity and depth location, using the *assign class* algorithm (Table 1). The plume was classified using a velocity of 4.075 km s^{-1} and a depth

of >225 km (Fig. 4a). The craton was classified using velocity values of 4.575 km s^{-1} for C3, and 4.375 km s^{-1} at a depth of ≤125 km for C1, and 4.475 km s^{-1} at a depth of ≤ 170 km for C2 (Fig. 4b).

In the next step, the rifts (R1–R3) were classified. For R1 and R2, the same approach was followed as for step 2. They were

classified based on their velocity values and depth (3.975 km s^{-1} for R1, and 4.075 km s^{-1} with a depth range of 120–200 km for R2), also using the *assign class* algorithm. Only the depth range was used to classify R2 and thereby prevented classifying other objects (P, RL1-2 and RC1-1) with the same velocity value, but at different depths (Fig. 3). To classify R3, a different approach was followed (*pixel-based object resizing*, Table 1). This was necessary due to the presence of PB1 with the same velocity and within the same depth range. The rift (R2) was allowed to grow vertically (−*Z*-direction only) and the growing was constrained to within the 4.175 km s^{-1} velocity class that was related to R3 of the rift (Figs 4i, j and c).

The fourth step focused on the surrounding horizontal layers (L1–L3). L1 was classified based on its velocity of 4.175 km s^{-1} and its depth of ≤125 km. This classification included segments that belonged to the boundaries between the craton and the rift (RC1-2) (Fig. 3). This misclassification was corrected using the *pixel-based object resizing* algorithm with the coating option in the *X*-direction. This was done by allowing the coating on the neighbourhood class of 4.275 km s^{-1}, which was classified as the original boundary class, as shown in Figs 4(k), (l), (m) and (d). L2 and L3 were classified in a similar way, using the *pixel-based object resizing* algorithm with the coating option, but in the −*Z*-direction. The segments below L1 were classified into L2 (Figs 4n and e), and the pixels below L2 were classified into L3 (Figs 4o, p and f).

In the last step, the boundaries were classified. The plume boundaries (PB1–PB3) have velocity values of 4.175, 4.275 and 4.375 km s^{-1}, respectively. PB1 and PB2 with 4.175 and 4.275 km s^{-1} velocity, respectively, were classified using the *pixel-based object resizing* algorithm with coating only in the +*Z*-direction (Fig. 4q). This way pixels coating the plume, and with velocity values equal to 4.175 and 4.275 km s^{-1}, were classified into the plume boundaries class (Fig. 4r). The remaining part of the plume boundary of 4.375 km s^{-1} was mixed with the rift boundary. To separate this remaining part of the plume boundaries, first the other rift boundaries needed to be classified. The largest part of the rift boundaries (velocity values of 4.025, 4.075, 4.125, 4.175, 4.225,

4.275 and 4.325 km s^{-1}) was classified using the *assign class* algorithm. Also, the segments of the 4.375 km s^{-1} class with a shallow location (<190 km) were classified into rift boundaries (Fig. 4r). The remaining parts of the plume boundaries in the mixed boundaries zone were classified using the *pixel-based object resizing* algorithm with a growing option in the +*Z*-direction, and limiting the growing process to 2 pixels only to prevent including upper pixels that belonged to the rift boundaries (Fig. 4r). Everything remaining afterwards with a velocity of 4.375 km s^{-1} was assigned to the rift boundaries (Fig. 4s). The complete 3-D rift boundaries and plume boundary can be seen in Figs 4(g) and (h), respectively.

The final model mimics the input model perfectly, using a semi-automatic approach in which we only needed number of thresholds to be fed in the pre-defined segmentation/classification algorithms of eCognition. However, the interpretation was accomplished in an approach similar to cognitive visual image analysis. The four main classes were accurately resolved. The gradual boundaries were the most challenging part in the classification process, due to their overlap in velocity and depth with the four main features. In reality, boundaries are fuzzy. The information on them, and possibly also on the main features, might not be known *a priori*. However, this additional challenge can be satisfactorily solved as shown for the 3-D seismological model in the next section.

4.2 3-D OOA of real seismological model

The approach for the 3-D seismological model is similar to the one followed for the synthetic model. Due to different boundary conditions and the available *a priori* information, however, the steps were done in a different order and with different thresholds. Thresholds were again based on the analysis of the 3-D histogram of the seismological model supported by visual interpretation and the *a priori* knowledge from the interpretation of the model of Adams *et al.* (2012, Fig. 5). The main features and their boundaries were defined and used to set the corresponding thresholds.
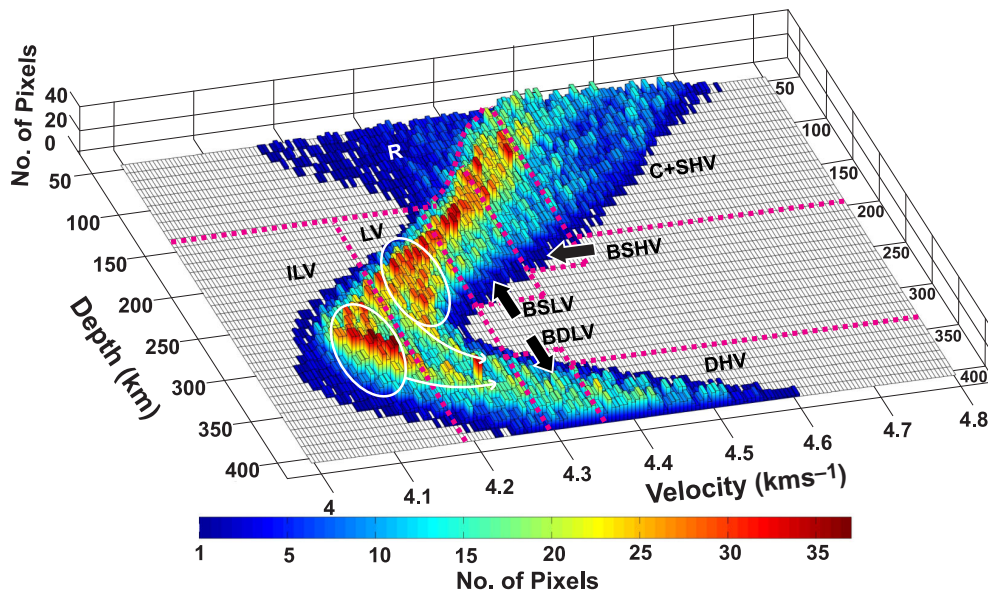

Figure 5. 3-D histogram explaining the process of the object extraction based on the objects' velocity values and their depth. Rifts (R), craton (C), shallow high velocity (SHV), boundary shallow high velocity (BSHV), boundary shallow low velocity (BSLV), low-velocity zone (LV), inner low-velocity zone (ILV), boundary deep low velocity (BDLV) and deep high velocity (DHV). The white circles indicate the two anomaly clusters of the low-velocity zone (LV), and (ILV) and the white curved arrows indicate the decay of these anomaly clusters towards the boundary deep low-velocity zone (BDLV).

A low-velocity zone was defined on the histogram by its velocity (<4.292 km s^{-1}) and location (depth $>\sim150$ km). The zone was split into an outer (LV) (4.18–4.29 km s^{-1}) and inner (ILV) (<4.18 km s^{-1}) part based on the presence of two separate low-velocity clusters around 4.25 and 4.13 km s^{-1}, respectively, as shown by the white circles in Fig. 5. The rifts showed a characteristic low velocity in the shallow zone (Fig. 5). They were defined by a depth and velocity ranging from 4.18–4.47 km s^{-1} at 50-km depth, to 4.28–4.32 km s^{-1} at 140-km depth. This low-velocity zone was differentiated from other objects in the shallow part of the model by its diffuse character, a zone marked by low counts (frequency) in a broad range of depths and velocities. The craton and high-velocity zone in the shallow part (SHV) have a high velocity (4.47–4.74 km s^{-1}) and a depth of $>\sim190$ km. The zone surrounding these objects was defined as a fuzzy high-velocity boundary (BSHV) and a transition between the high-velocity objects (Fig. 5). A similar fuzzy boundary was identified between the deep low-velocity zone and the rifts, and is indicated in Fig. 5 as a boundary shallow low velocity (BSLV). This boundary was too fuzzy to set a specific velocity range, thus the threshold to define these two boundaries zones was determined by taking the intermediate velocity between the high and low-velocity objects (4.37 km s^{-1}). Another deep high-velocity zone (DHV) exists below the low-velocity zone (LV and ILV). It has the same velocity characteristics in the 3-D histogram (velocity >4.4 km s^{-1}) as the shallow-high velocity objects, but is located at a depth $>\sim340$ km. The boundaries between this object and the deep low velocity object (BDLV) were determined based on the decay of the two low-anomaly clusters (Fig. 5). The final threshold was 4.29 km s^{-1}.

The final ruleset consists here of six steps. Due to the increased fuzziness, different steps were taken to define the objects compared to the synthetic example. The maximum velocity in the model was 4.74 km s^{-1}, and the minimum 4.05 km s^{-1}. Adams *et al.* (2012) used 10 classes (4.15–4.65 km s^{-1} with 0.05 km s^{-1} interval) to analyse the model.

In the first step, the image stack was classified into 26 velocity classes (4.05–4.75 km s^{-1} with ~0.03 km s^{-1} interval), to increase the smoothness of objects only without adding any artefacts to the original data.

Step 2 classified the deep high-velocity object (DHV) and its boundary (BDLV), using the *assign class* algorithm. The thresholds for the deep high-velocity zone were a velocity of >4.37 km s^{-1} and a depth of >340 km. The boundary was classified using a velocity range of 4.29–4.37 km s^{-1} and a depth >300 km (Figs 6a and b).

The low-velocity zone was classified in step 3 based on its low velocity (4.05–4.29 km s^{-1}) and deep location (depth >150 km). The inner part (ILV) was first defined based on a velocity of <4.18 km s^{-1} (Fig. 6c). The outer part (LV) was composed of the remainder with a velocity of 4.18–4.29 km s^{-1} (Fig. 6d).

In the fourth step, the rift (R) was classified based on its low velocity and shallow depth. Both depth and velocity were defined in ranges to cover the fuzzy characteristics of this object (4.18–4.47 km s^{-1} at 50-km depth, to 4.28–4.32 km s^{-1} at 140-km depth). A sequence of *assign class* algorithm steps was applied to define the velocity range at each depth (Fig. 6f).

Step 5 focused on classifying the craton (C) and the high-velocity zones (SHV) in the shallow part of the model (50–200 km and 4.47–4.74 km s^{-1}) into two objects. The first is the craton located within the rift branches. It was defined using a small part of the depth range (50–80 km) with the highest velocity in the model that was characteristic for the craton only (4.67–4.74 km s^{-1}). It was then allowed to grow in the *X, Y* and *Z*-directions until it filled the craton's

Deep high velocity (DHV) | **Boundary deep low velocity (BDLV)**

Inner low velocity (ILV) | **Low velocity (LV)**

Boundary shallow low velocity (BSLV) | **Rift (R)**

Boundary shallow high velocity (BSHV) | **Craton (C)** | **Shallow high velocity (SHV)**
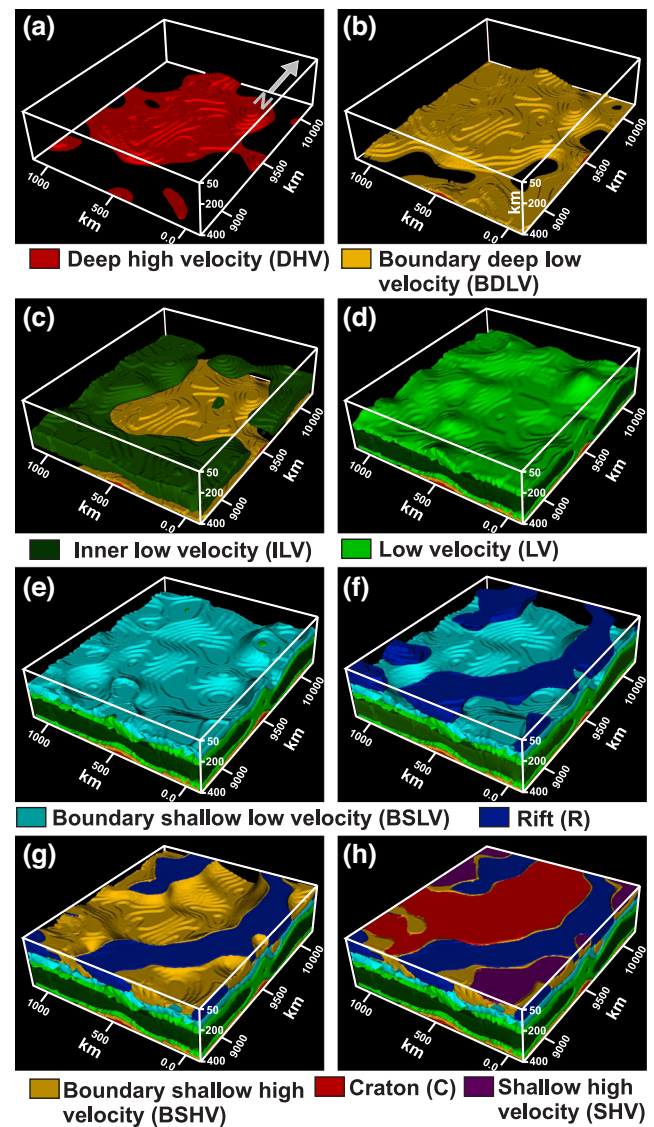
Figure 6. 3-D OOA of the real model. Panels (a–h) show the 3-D OOA extraction process where (a) illustrates the deep high-velocity object (DHV), (b) the boundary deep low-velocity (BDLV), (c) the inner low velocity zone (ILV), (d) the outer part of the low-velocity zone (LV), (e) the boundaries of the shallow low velocity (BSLV), (f) the rifts (R), (g) the boundaries of the high-velocity objects (BSHV) and (h) the craton (C) and the shallow high-velocity objects (SHV).

central main part. The remaining high velocities were assigned to the high-velocity zone surrounding the rift. The extracted craton and the shallow high-velocity zone can be seen in Fig. 6(h).

The final step classified the high (BSHV) and low-velocity (BSLV) boundaries using the *assign class* algorithm based on their velocity ranges 4.29–4.37 km s^{-1} for the low-velocity boundary (Fig. 6e), and 4.37–4.47 km s^{-1} for the high-velocity boundary (Fig. 6g).

The resulting model (Fig. 6h) showed the possibility to resolve objects that are known to be present in the region based on *a priori* knowledge, which were as much as possible translated into objective criteria. The uncertainty of the extracted objects is related to the uncertainty of the shear wave seismic tomography model, which ranged from 25 to 50 km for the depths between 50–250 km and 75–100 km for deeper depths. Difficulties in the classification

process were mainly confined to boundary zones, similar to what was observed for the synthetic model. The real conditions were more challenging to resolve than in the synthetic case, since the boundaries did not have sharp and clear characteristics in the 3-D histogram and were visually not easily identifiable. Therefore, the boundaries of the objects were defined in separate classes (Figs 6b, e and g). These separate classes allowed a degree of freedom to describe the fuzzy characteristic of the objects and helped in identifying the body of the main objects.

An issue to be aware of for future use was that eCognition showed the model as a mirror image around the *Y* (north–south) axis of the model. However, this was only a visualization issue since the exported sections and depth slices had a correct orientation and georeferenced position.

5 DISCUSSION AND CONCLUSIONS

3-D OOA demonstrated the possibility to extract meaningful objects from 3-D geophysical data in a semi-automatic way, in which the user does not need to interpret objects manually. The approach allows for a semi-objective setting of thresholds that can be tested and, if necessary, changed in a very fast and efficient way. These changes require only changing the thresholds used in the ruleset or by defining additional algorithms to be included in the ruleset for the extraction process.

The results of the synthetic model analysis showed the capability of 3-D OOA to retrieve 3-D objects from geophysical data. The extraction process of the main objects [craton, rift, plume and the three horizontal layers (Fig. 4)] required a classification based on the velocity and depth values. However, the combination of dividing the objects into zones and their gradual boundaries added complexity to the objects configurations and to the object retrieving process, since there are different parts in different objects that have the same velocity values. This made an object extraction process for these objects based on the velocity values and depths alone impossible. Moreover, it showed the need for the *pixel-based object resizing* algorithm, and specifically the growing and coating options, in order to define the objects. With this approach it was possible to define objects in conditions where the object boundaries were not well-defined and fuzzy, such as the mixed zone of the rift and plume boundaries. The synthetic model analysis was driven by the *a priori* knowledge on the objects present in the model. Also the object characteristics and thresholds were well defined in the 3-D histogram. As expected, the 3-D histogram of the real data was substantially more complex. Furthermore, for the real scenarios no knowledge of the actual object densities and depths may be available.

The real model results showed how 3-D OOA can deal with realistic 3-D subsurface conditions in which the boundaries become fuzzy, the object extensions become unclear and the model characteristics vary with depth due to the different physical conditions going from shallow to large depths in the subsurface. The 3-D OOA-derived objects, the rifts, the craton, the low-velocity zone and the deep high-velocity zone (Fig. 6), were extracted based on their velocity and their depth location. However, most of the objects boundaries have strong fuzzy characteristics and it was not straightforward to define objective measures for accurate definition of these boundaries. This was solved by using separate classes to define the objects boundaries which give more confident to the major classified objects. However, the process to define fuzzy boundaries in a seismological model needs further research to reduce non-uniqueness in the definition of these boundaries. The smooth transition between

objects and their surroundings is often too fuzzy to be mapped with confidence. However, eCognition is fundamentally also based on the concept of fuzzy classification. This means that segments marked by value transitions, and that may thus belong to more than one class, can also be classified as such. Moreover, a *multiresolution segmentation* algorithm (Baatz & Schäpe 2000; Baatz *et al.* 2005) can be used instead of the *multithreshold segmentation* algorithm since it can deal with complex structures which have different scales. However, the selection of the optimum scale parameter is a challenging task, even when using the Estimate Scale Parameter (ESP) tool (Drăguţ *et al.* 2010) which requires further extension to allow the processing of 3-D data. The same is true for another approach for objective segmentation parameter identification, the Plateau Objective Function by Martha *et al.* (2011).

The main geophysical application for 3-D OOA is any 3-D inversion and/or interpretation process. With the boundaries defined, both spatially as well as in depth, an inversion process can be more focused on retrieving actual properties and reducing the degrees of freedom for changing the shape of objects. This might be particularly useful for the inversion of potential field data where lateral variations are often reasonably well modelled but the depth resolution is very poor, thereby leaving a large degree of uncertainty on the final model in both object boundaries and property characteristics. A case study implementation for reducing non-uniqueness in satellite gravity inversions is shown by Fadel *et al.* (2013). This also might be particularly relevant for recent satellite gravity studies which use seismic tomography models (for a review, see van der Meijde *et al.* 2013b). A clear example where this might be of added value is the crustal thickness modelling in Africa (Tugume *et al.* 2013) and South America (van der Meijde *et al.* 2013a). In these studies, uniform densities were assumed throughout the continent, due to lack of objective and spatially homogeneous information. Spatially defined boundaries, based on density variations, can improve the modelling with spatially dependent density information. With 3-D OOA, the uncertainty on objects and physical properties can be potentially significantly reduced.

The eCognition rulesets developed in this research will be made available on our website www.itc.nl/ooa-group.

REFERENCES

Adams, A., Nyblade, A. & Weeraratne, D., 2012. Upper mantle shear wave velocity structure beneath the East African plateau: evidence for a deep, plateauwide low velocity anomaly, *Geophys. J. Int.,* **189**(1), 123–142.

Baatz, M. & Schäpe, A., 2000. Multiresolution segmentation: an optimization approach for high quality multi-scale image segmentation, in *Angewandte Geographische Informationsverarbeitung XII,* pp. 12–23, eds Strobl, J., Blaschke, T. & Griesebner, G., Wichmann.

Baatz, M., Schäpe, A., Schmidt, G., Athelogou, M. & Binnig, G., 2005. Cognition network technology: object orientation and fractal topology in biomedical image analysis. Method and applications, in *Fractals in Biology and Medicine,* Mathematics and Biosciences in Interaction, pp. 67–73, eds Losa, G., Merlini, D., Nonnenmacher, T. & Weibel, E., Birkhäuser.

Bauer, K., Muoz, G. & Moeck, I., 2012. Pattern recognition and lithological interpretation of collocated seismic and magnetotelluric models using self-organizing maps, *Geophys. J. Int.,* **189**(2), 984–998.

Bedrosian, P., 2007. MT+, integrating magnetotellurics to determine Earth structure, physical state, and processes, *Surv. Geophys.,* **28**(2–3), 121–167.

Bedrosian, P.A., Maercklin, N., Weckmann, U., Bartov, Y., Ryberg, T. & Ritter, O., 2007. Lithology-derived structure classification from the joint interpretation of magnetotelluric and seismic models, *Geophys. J. Int.,* **170**(2), 737–748.

Blaschke, T., 2010. Object based image analysis for remote sensing. *ISPRS J. Photogramm. Remote Sens.,* **65**(1), 2–16.

Bosch, M., 1999. Lithologic tomography: from plural geophysical data to lithology estimation, *J. geophys. Res.,* **104**(B1), 749–766.

Drăguţ, L., Tiede, D. & Levick, S.R., 2010. ESP: a tool to estimate scale parameter for multiresolution image segmentation of remotely sensed data, *Int. J. Geogr. Inf. Sci.,* **24**(6), 859–871.

Ebbing, J., Braitenberg, C. & Götze, H., 2001. Forward and inverse modelling of gravity revealing insight into crustal structures of the Eastern Alps, *Tectonophysics,* **337**(3–4), 191–208.

eCognition Developer, 2011a. eCognition Developer 8.7 Reference Book. Trimble Germany GmbH, Trappentreustr., Munich, Germany.

eCognition Developer, 2011b. eCognition Developer 8.7 User Guide. Trimble Germany GmbH, Trappentreustr., Munich, Germany.

Fadel, I., van der Meijde, M., Kerle, N. & Lauritsen, N., 2013. 3D object-oriented image analysis in 3D geophysical modelling: analysing the central part of the East African Rift System, *Int. J. appl. Earth Obs. Geoinf.,* http://dx.doi.org/10.1016/j.jag.2013.11.004.

Gallardo, L.A. & Meju, M.A., 2011. Structure-coupled multiphysics imaging in geophysical sciences, *Rev. Geophys.,* **49**(1), doi:10.1029/2010RG000330.

Götze, H. & Lahmeyer, B., 1988. Application of three-dimensional interactive modeling in gravity and magnetics, *Geophysics,* **53**(8), 1096–1108.

Guillen, A., Calcagno, P., Courrioux, G., Joly, A. & Ledru, P., 2008. Geological modelling from field data and geological knowledge: part II. Modelling validation using gravity and magnetic data inversion, *Phys. Earth planet. Inter.,* **171**(1–4), 158–169.

Infante, V., Gallardo, L.A., Montalvo-Arrieta, J.C. & de Len, I.N., 2010. Lithological classification assisted by the joint inversion of electrical and seismic data at a control site in northeast Mexico, *J. appl. Geophys.,* **70**(2), 93–102.

Kerle, N. & de Leeuw, J., 2009. Reviving legacy population maps with object-oriented image processing techniques, *IEEE Trans. Geosci. Remote Sens.,* **47**(7), 2392–2402.

Li, X., 2010. Efficient 3D gravity and magnetic modeling, In *Proceedings of EGM 2010 International Workshop,* Capri, Italy, Expanded Abstracts.

Martha, T., Kerle, N., van Westen, C., Jetten, V. & Kumar, K., 2011. Segment optimization and data-driven thresholding for knowledge-based landslide detection by object-based image analysis, *IEEE Trans. Geosci. Remote Sens.,* **49**(12), 4928–4943.

Sanchez, J., Götze, H. & Schmitz, M., 2011. A 3-D lithospheric model of the Caribbean-South American plate boundary, *Int. J. Earth Sci.,* **100**(7), 1697–1712.

Schmidt, S., Götze, H., Fichler, C. & Alvers, M., 2010. IGMAS+: a new 3D gravity, FTG and magnetic modelling software, Extended abstract, *Geoinformatik,* 57–63.

Schönmeyer, R., Prvulovic, D., Rotarska-Jagiela, A., Haenschel, C. & Linden, D.E., 2006. Automated segmentation of lateral ventricles from human and primate magnetic resonance images using cognition network technology, *Magn. Reson. Imaging,* **24**(10), 1377–1387.

Stumpf, A. & Kerle, N., 2011. Object-oriented mapping of landslides using random forests, *Remote Sens. Environ.,* **115**(10), 2564–2577.

Tugume, F., Nyblade, A., Juliá, J. & van der Meijde, M., 2013. Precambrian crustal structure in Africa and Arabia: evidence lacking for secular variation, *Tectonophysics,* **609**, 250–266.

van der Meijde, M., Juliá, J. & Assumpão, M., 2013a. Gravity derived Moho for South America, *Tectonophysics,* **609,** 456–467.

van der Meijde, M., Pail, R., Bingham, R. & Floberghagen, R., 2013b. GOCE data, models, and applications: a review, *Int. J. Appl. Earth Obs. Geoinf.,* http://dx.doi.org/10.1016/j.jag.2013.10.001.

Willhauck, G., 2012. eCognition community, 3D LiDAR Point Cloud Analysis. Available at: http://community.ecognition.com/home/ecognition-labs/3d-lidar-point-cloud-analysis/?searchterm=3D (last accessed 7 June 2013).

SUPPORTING INFORMATION

Additional Supporting Information may be found in the online version of this article:

Appendix S1. 3-D object rulesets

(http://gji.oxfordjournals.org/lookup/suppl/doi:10.1093/gji/ggu137/-/DC1).

Please note: Oxford University Press is not responsible for the content or functionality of any supporting materials supplied by the authors. Any queries (other than missing material) should be directed to the corresponding author for the article.